Significant enhancements of the mesospheric Na layer bottom below 75 km observed by a full-diurnal-cycle lidar at Beijing (40.41 N, 116. 01 E), China

Yuan Xia [1,2], Jing Jiao [2], Satonori Nozawa [3], Xuewu Cheng [4], Jihong Wang [2], Chunhua Shi [5], Lifang Du [2], Yajuan Li [1], Haoren Zheng [2], Faquan Li [4], Guotao Yang [2]

[1] School of Electronic Engineering, Nanjing Xiaozhuang University, Nanjing, 211171, China
[2] State Key Laboratory of Space Weather, National Space Science Center, Chinese Academy of Sciences, Beijing, 100190, China
[3] Institute for Space-Earth Environmental Research, Nagoya University, Nagoya, 464-8601, Japan
[4] Innovation Academy for Precision Measurement Science and Technology, Chinese Academy of Sciences, Wuhan, 430071, China
[5] School of Atmospheric Sciences, Nanjing University of Information Science and Technology, Nanjing, 210044, China

Correspondence to: Guotao Yang (gtyang@nssc.ac.cn)

Abstract. Based on the full-diurnal-cycle sodium (Na) lidar observations at Beijing (40.41 N, 116.01 E), we report pronounced downward extensions of the Na layer bottomside to below 75 km near mid-December, 2014. Considerable Na atoms were observed even as low as ~72 km, where Na atoms is short-lived. More interestingly, an unprecedented Na density of ~2500 atoms/cm^3 around 75 km was observed on December 17, 2014. Such high Na atoms concentration was two orders of magnitude larger than that normally observed at the similar altitude region. The variations of Na density on the layer bottom were found to be accompanied by warming temperature anomalies and considerable perturbations of minor chemical species (H, O, O$_3$) in the upper mesosphere. Different from the previous reported metal layer bottom enhancements mainly contributed by photolysis after sunrise, these observational results suggest more critical contributions were made by the Na neutral chemical reactions to the Na layer bottom extensions reported here. The time-longitudinal variations of background atmospheric parameters in the upper mesosphere and stratosphere from global satellite observations and ERA reanalysis data indicated that the anomalous structures observed near the lidar site in mid-December, 2014 were associated with planetary wave (PW) activities. The anomalies of temperature and O$_3$ perturbation showed opposite phase in the altitude range of 70~75 km and 35~45 km. This implied that the vertical coupling between the mesosphere and stratosphere, possibly driven by the interactions of PW activities with background atmosphere and modulation of gravity wave (GW) filtering by stratospheric wind, contributed to the perturbations of background atmosphere. Furthermore, the bottom enhancement on December 17, 2014 was also accompanied by clear wavy signatures in the main layer. The strong downwelling regions are likely due to the superposition of tide and GW, suggesting the wave-induced adiabatic vertical motion of the air parcel contributed greatly to the formation of the much stronger Na layer bottom enhancement on December 17, 2014. These results provide a clear observational evidence for the Na layer bottom response to the planetary-scale atmospheric perturbations in addition to tide and GW through affecting the chemical balance. The results of this paper

35   also have implications for the response of the metal layer to vertical coupling between the lower atmosphere and the mesosphere.

1 Introduction

Metallic layers in the mesosphere and lower thermosphere (MLT) region are good tracers for studying atmospheric dynamics and photochemistry. The neutral sodium (Na) layer is generally observed in altitude range of 80~110 km. Different from the

40   usually gentle upper edge, the absolute value of Na density vertical gradient around lower edge is relatively large, and Na atoms concentration sharply decreases below 80 km where Na atoms are extremely short-lived (Xu and Smith, 2003). This is mainly because most of the neutral metal atoms below 80 km are oxidized by O_3 and finally converted to reservoir species (mainly $NaHCO_3$) through a series of chemical reactions (Plane, 2004; Plane et al., 2015). $NaHCO_3$ is eventually removed mainly through dimerization and the permanent attachment of the Na species onto meteoric smoke particles.

45   Na layer observations over a full diurnal cycle enable the investigations on the diurnal variation of Na density and the role of tidal wave modulations in the Na diurnal and semidiurnal variations (States and Gardner, 1999; Clemesha et al., 2002; Yuan et al., 2012, 2014). On the bottom side of the Na layer, photochemical reactions are recognized playing important roles in the Na diurnal variation (Plane et al., 1999; Yuan et al., 2019). Photolysis and neutral chemical reactions can convert $NaHCO_3$ back to Na atoms on the Na layer bottom, but the latter are greatly decelerated by the sharp drop of the

50   concentrations of atomic O and H below 80 km (Plane et al., 2015).

Considerable increases in Na density on the layer underside near 80 km after sunrise were previously reported by Yuan et al. (2019). The dominant contribution of solar radiation-induced photolysis of the major reservoir species $NaHCO_3$ on the daytime Na layer bottom enhancement was suggested by combining with simulation by Whole Atmosphere Community Climate Model with Na chemistry (WACCM-Na) (Marsh et al., 2013). It is worth mentioning that the diurnal variation on

55   the Na layer bottom is generally not as pronounced as observed on the Fe layer bottom. For instance, daytime Na density below 80 km is generally two orders of magnitudes lower than that around the main layer peak (States and Gardner, 1999; Yuan et al., 2019), while Fe density around its daytime lower edge below 75 km can reach to more than 10% of the layer peak density, as reported in Yu et al. (2012) and Viehl et al. (2016). Besides, during daytime, considerable Fe atoms were observed as low as ~72 km, several kilometers lower than the generally observed lower edge of Na layer. Sometimes, the

60   increase of Na density around 80 km is even within its natural variability on the layer bottom. Yuan et al. (2019) suggested that faster density increase of Fe than Na on the layer bottom after sunrise is mainly due to the much higher rate coefficients of photolysis of FeOH (determined to be $J(FeOH)=(6 \pm 3) \times 10^{-3}$ s^{-1} by Viehl et al. (2016)) compared with that of $NaHCO_3$ ($J(NaHCO_3)=1.3 \times 10^{-4}$ s^{-1} according to Self and Plane (2002)). In addition, Na atoms have higher rate of oxidation by O_3 and lower rate of liberation from the main reservoir species by reaction with H than Fe atoms (Plane et al., 2015), which could

65   further contribute to the less significant diurnal variation on the Na layer underside.

In this paper, we report significant enhancements of the Na layer below 75 km observed in mid-December, 2014 by a full-diurnal-cycle Na lidar at Beijing (40.41 °N, 116.01 °E). Na atoms concentration was greatly enhanced in the altitude range of 70~75 km, where Na atoms generally have extremely short lifetime. Of greater interest is the observation of an unprecedented Na bottom enhancement with ~2500 atoms/cm^3 around 75 km on December 17, 2014. Such large Na density is comparable to the peak density of the normal main layer between 80 and 105 km. The variation of the Na layer bottom is inconsistent with that of solar zenith angle, implying that other mechanisms, instead of photolysis, make a more critical contribution. The possible formation mechanisms for the significant Na density enhancements on the layer bottom between 70 and 75 km are discussed combining with the results of background atmospheric parameters from global satellite observations, a nearby meteor radar, and reanalysis data.

2 Instrument and Data

2.1 Na Lidar

The broadband Na resonant fluorescence lidar of Chinese Meridian Project in Yanqing, Beijing (40.41 °N, 116.01 °E) permits full-diurnal continuous observation of Na layer when weather is permitted. By utilizing narrowband Faraday anomalous dispersion optical filters (FADOF) in the lidar receivers, the strong background light during the daytime can be effectively suppressed (Chen et al., 1996). The spatial and temporal resolution of raw data were 96 m and 33.3 s (corresponding to 1000 laser pulses integrated to produce a profile), respectively. The raw data was further integrated within 15 min and a Hanning window filtering with 960 m full width at half maximum (FWHM) was employed in height. The main parameters of the lidar system can be found in the published papers (Wang et al., 2010; Jiao et al., 2015; Xia et al., 2020). The diurnal operations of Na lidar have been conducted from April, 2014 and more than 4500 hours of observational data were collected covering four seasons. In this study, the Na lidar observational data in December, 2014 was used.

2.2 TIMED/SABER satellite, Meteor radar and reanalysis data

In order to investigate possible mechanisms for the unusual Na layer bottom enhancements below 75 km, we used the measurement results of atmospheric temperature and Na-chemistry related atmospheric minor species (e.g., H, O, O$_3$) from the Sounding of Atmosphere using Broadband Emission Radiometry (SABER) onboard Thermosphere, Ionosphere, and Mesosphere Energetics Dynamics (TIMED) satellite (Russell III et al., 1999). TIMED satellite was launched on December 2001, and SABER instrument measurements can provide vertical profiles of atmospheric parameters, e.g., temperature, pressure, geopotential height, volume mixing ratios (VMRs) of the trace species O$_3$, CO$_2$, H$_2$O, O, and H with an interval of ~0.4 km. In general, two sampling profiles can be obtained in one day for a given site. In this study, we analyzed the SABER data (H, O, and O$_3$) in December, 2014 within ~±5 ° latitude (35-45 °N) and longitude (110-120 °E) of the Na lidar location, and compared to the zonal mean values within the latitude range of 35-45 °N. The atmospheric parameters in different

longitudes within 35-45 °N were also used to analyse their longitudinal variations (Data source: http://saber.gats-inc.com; v2.0; Level 2A).

The zonal wind data in MLT region (70-110 km) from a meteor radar (40.3 °N, 116.2 °E) near the lidar site as well as the stratospheric zonal wind from ERA-Interim reanalysis data of the European Center for Medium-Range Weather Forecasts (ECMWF) were also used. The meteor radar is operated by the Institute of Geology and Geophysics, Chinese Academy of Sciences (IGGCAS) (Yu et al., 2013). The zonal wind data obtained from meteor radar has a resolution of 2 km in altitude and 1 h in time. ERA-Interim is a global atmospheric reanalysis that is available from 1 January 1979 to 31 August 2019. It covers 37 pressure levels from 1000 to 1 hPa and can provide 4 time points with a step of 6 h. In this study, we selected a grid with a resolution of 3 °(latitude)×3 °(longitude). ERA-Interim data were downloaded through ECMWF at https://www.ecmwf.int/en/forecasts/datasets/archive-datasets/. In addition, the amplitudes of PWs of zonal wave numbers 1 (PW1) and 2 (PW2) in geopotential height at 10 hPa, 60 °N were obtained from the NASA online data service (https://acd-ext.gsfc.nasa.gov/Data_services/met/ann _data.html).

3 Observational Results

Figures 1(a, c) show the local time and height evolution of Na density at logarithmic scale with temporal resolution of 1 h and height resolution of 960 m. The X-axis represents the date in December, 2014. The white sectors represent there are not valid observational data. The red dotted curves represent the variations of solar zenith angle. From the contour plots in Figure 1 we can clearly see nearly regular daytime extensions near 80 km during almost all the available observational days. As the daytime increase of Na atoms density on the layer bottom is relatively low, it could be easily overlooked when plotted with a linear scale (States and Gardner, 1999). Compared to the results observed in autumn from a similar middle latitude (41.8 °N, 111.8 °W) by Yuan et al. (2019), the bottom enhancements of Na layer around 80 km presented in Figure 1 are more apparent. This is most likely due to the warmer mesopause in winter month, which can accelerate the neutral chemical reactions converting the metal reservoirs back to the metal atoms.
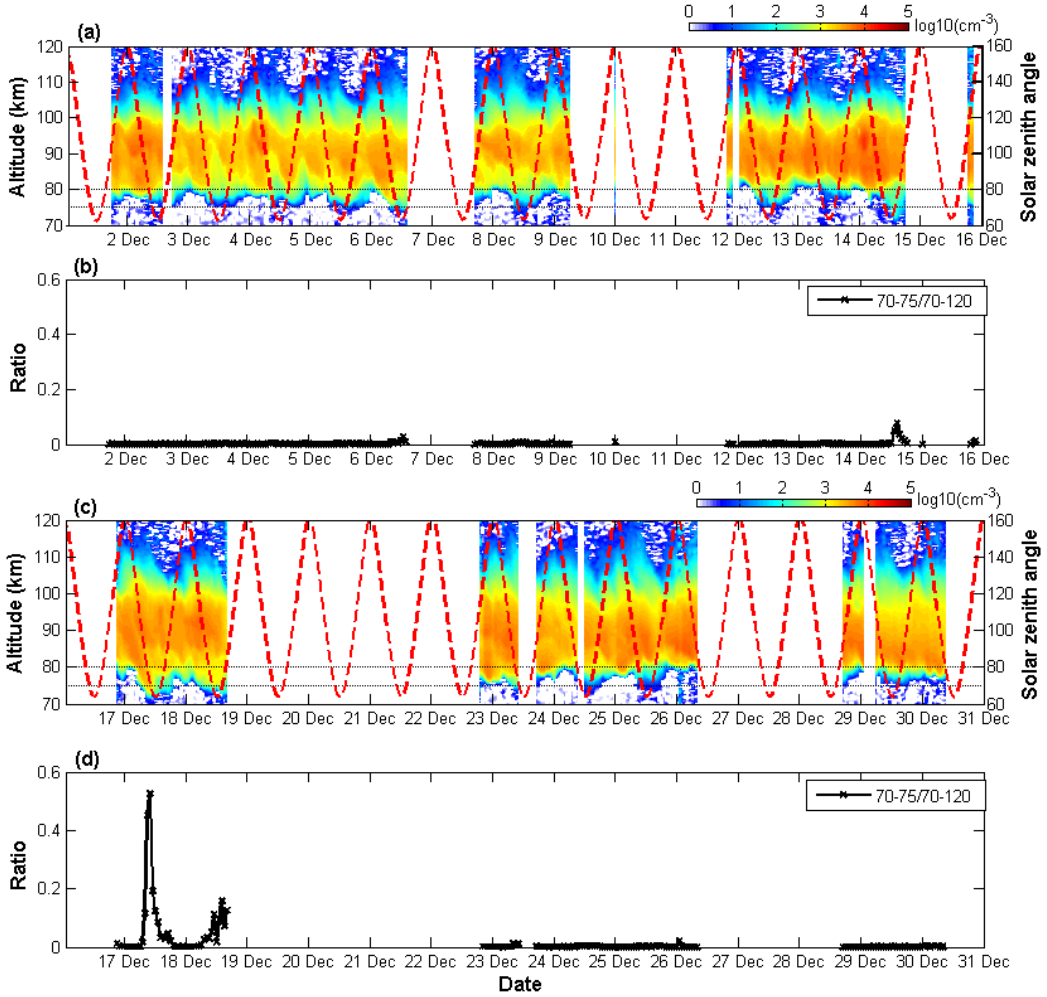
Figure 1: (a, b) The time-height evolution of Na density and the corresponding temporal variation of the ratio of Na density averaged in the altitude range of 70-75 km to that within 70-120 km on December 3-9, 2014. **(c, d)** The same but on December 12-18, 2014. The solar zenith angle is plotted with red dotted curves in (a) and (c). The two black dashed lines in (a) and (c) denote 80 km and 75 km, respectively.

Noteworthy is the much more significant bottom enhancements below 75 km observed in mid-December (i.e., on 14, 17 and 18 December, there are data gaps during 15-16 December), as can be seen in Figures 1(a, c). The pronounced Na bottom enhancements between 70 and 75 km on 14, 17 and 18 December are also shown in Figures 1(b, d) by the temporal variation of the ratio of Na density averaged within 70-75 km to that within 70-120 km. The most intriguing result appears in the early morning of December 17, when Na atom density around 75 km even reaches up to the same order of magnitude as the peak density of the Na main layer.
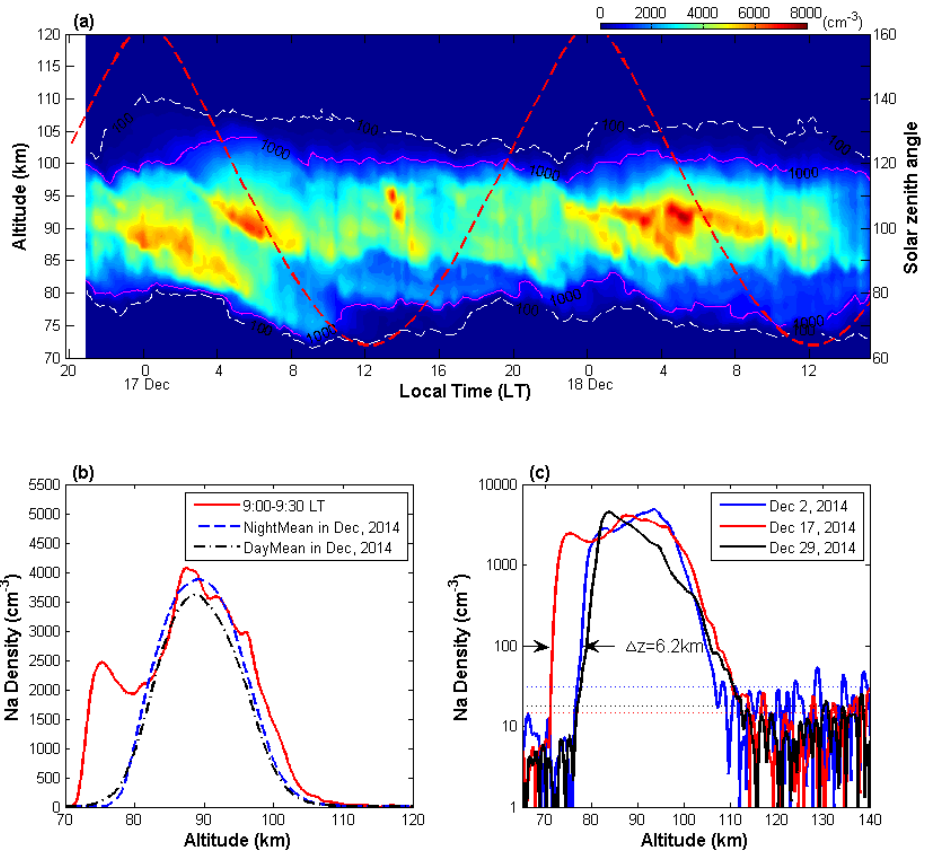
Figure 2: (a) Contours of Na density versus local time and altitude observed from ~21 LT on December 16 to ~16 LT on December 18, 2014. The time resolution is 15 min, and altitude resolution is 960 m. (b) Comparison of Na density profiles averaged at 9:00-9:30 LT on December 17 (red solid line), and averaged during daytime (7:00-17:00 LT, black dotted line) and nighttime (17:00-07:00 LT, blue dashed line) in December, 2014. (c) Comparison of Na density profiles on December 17 (red curve) with those on December 2 (blue curve) and 29 (black curve). The horizontal dotted lines are their respective detection limits, whose values from small to large are ~15 cm^{-3}, 19 cm^{-3}, 31 cm^{-3}.

Figure 2a shows the Na density contour in time-altitude over about 43 h from ~21 LT on December 16 to ~16 LT on December 18, 2014 in a linear scale. The variation of the solar zenith angle is also plotted with red dashed line. It can be seen that the constant density line of 100 cm^{-3} (white dashed line) on the Na layer bottom moves downward from ~80 km before 4 LT to ~71.5 km around 9:15 LT on December 17, then it oscillates at this lower altitude until ~17 LT when it begins to recover upward to above 75 km. The constant density line of 1000 cm^{-3} (pink solid line) on the layer bottom shows a similar downward movement in the early morning of December 17, and reached to its lowest altitude at ~72 km around 9:15 LT, however, it rapidly recovered upward by over 5 km at around 11:00 LT. Figure 2b displays the vertical profile of Na number density averaged at 9:00-9:30 LT on December 17 (red solid line), along with the averaged nocturnal and daytime Na profiles in December, 2014 (blue dashed and black dotted lines, respectively). It clearly shows the pronounced Na

145 density enhancement below 80 km on December 17. The Na density around 75 km reaches to ~2500 cm^{-3}, which is nearly two orders of magnitude larger than the daytime mean value of this month at a similar altitude. This implies interesting and complicated atmospheric physical and chemical processes. In order to further clarify the very significant bottom enhancement on December 17, in Figure 2c we also compared the Na density profile on December 17 (red curve) with those on December 2 (blue curve) and 29 (black curve), which can represent the cases in the early and late December, respectively.

150 The Na density profiles in Figure 2c are also the results averaged at 9:00-9:30 LT for each day and plotted in logarithmic coordinate. The dotted lines are their respective detection limits that are given by 1.5 times of the standard deviation of the background noise (Gao et al., 2015). The detection limit for the density profile on December 17 is ~15 cm^{-3}. The altitude difference between December 17 and the other two days is as large as ~6.2 km for the density of 100 cm^{-3}.

In the early morning of December 18, Na density increase on the layer underside below 75 km can also be seen, but it is

155 evident from Figure 2a that the bottom enhancement is less intense as compared to the previous day (December 17). It is noted that the Na main layer is also very different between the two adjacent days. The Na layer observations between 22 LT on December 16 and 12 LT on December 17 shows an apparent double-peak structure with downward phase propagation. The first peak which appears around 22 LT near 92 km descends at a rate of ~0.5 m/s. The second peak appears around 04 LT and 95 km, and also shows a similar downward propagation phase speed. The strong bottom extension in the morning of

160 December 17 follows well the downward propagation trend of the first peak in the main layer, but its peak density rapidly decreases below 80 km.

4 Discussion

The Na layer observational results presented in Section 3 reveal more significant bottom extensions as low as ~72 km in mid-December, 2014 (i.e., December 14, 17 and 18, as shown in Figure 1) compared to the normal results observed on other

165 days in December. Another noteworthy feature is the striking bottom enhancement with an unprecedented density of ~2500 cm^{-3} around 75 km in the morning of December 17.

Theories and model simulations of the metal layer (Cox et al., 2001; Plane 2004; Plane et al. 2015) indicated that the chemical lifetime of Na atoms near the Na layer peak is much longer than the time scale of vertical transport, thus the dynamical processes dominate the Na density variation between 85 and 95 km (Xu and Smith, 2003), while near the bottom

170 of Na layer, Na chemistry plays a more significant role (Self and Plane, 2002). According to Plane et al. (2015), here we simply describe the main Na chemical reactions that determine the Na variations on the bottom side of the layer:

$Na+O_3 \rightarrow NaO+O_2$ $\qquad$ $1.1 \times 10^{-9} \exp(-116/T)$ $\hfill$ (R1)

$NaHCO_3 + h\nu \rightarrow Na + HCO_3$ $\qquad$ 1.3×10^{-4} $\hfill$ (R2)

$NaHCO_3+H \rightarrow Na+H_2CO_3$ $\qquad$ $(1.84 \times 10^{-13})T^{0.777}\exp(-1014/T)$ $\hfill$ (R3)
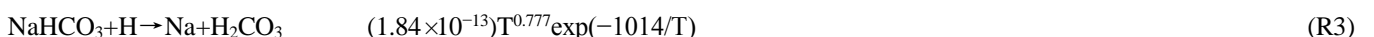
 units: unimolecular, s⁻¹; bimolecular,cm³ molecule⁻¹ s⁻¹

The neutral Na chemistry on the underside of the Na layer is mainly controlled by odd oxygen (O and O_3) and hydrogen (H) chemistry. Through oxidation reaction of Na with O_3, Na is converted to NaO (or further oxidized to NaO_2, NaO_3) (R1), which can further react with H_2O or H_2 and CO_2 (and O_2) to form the relatively stable $NaHCO_3$, which is believed to be the major reservoir species for Na (Plane et al., 2015; Gomez-Martin et al., 2016). The oxidation reaction of Na atoms (R1) is greatly accelerated with altitude decrease as it is sensitive to pressure (Yuan et al., 2019). NaO and NaO_2 produced by the oxidation are short-lived according to Self and Plane (2002). They can also be recycled back to Na by atomic O. As atomic O has a large positive vertical gradient near the mesopause region, the chemical lifetime of Na atoms is extremely short (only several seconds) on the underside of the Na layer around and below 80 km (Xu and Smith, 2005), and most of Na is in the form of $NaHCO_3$. This also results in a sharp lower edge of Na layer near 80 km.

During daytime, solar radiation will significantly accelerate the photolysis reaction of $NaHCO_3$, thus a part of $NaHCO_3$ can be converted back to Na atoms (R2). $NaHCO_3$ can also be recycled back to Na by reaction with H (R3). The reaction rate of $NaHCO_3$ with H positively depends on background temperature. The photolysis of O_2, O_3 and H_2O during the day can greatly increase the concentrations of atomic O and H around and below 80 km (Plane, 2003), thus further promoting the release of Na atoms from $NaHCO_3$ or NaO and NaO_2. Generally, the typical daytime H concentration is $\sim$2-5$\times10^7$ cm^{-3} between 75 and 80 km (Plane et al., 2015; Yuan et al., 2019), and mesopause temperature is $\sim$200 K, resulting in that the first-order rate of reaction R3 is dozens times slower than that of R2. Thus, photolysis reaction of $NaHCO_3$ is often considered to dominate the increase in Na concentration on the layer bottom after sunrise (Yuan et al., 2019). Photolysis of other Na species can also contribute to Na density increase. However, the bottom extensions downward to $\sim$72 km are not seen in early and late December even though the variation of solar illumination with local time is similar in the same month. Moreover, the variations of Na layer bottom on December 17 are inconsistent with that of solar zenith angle. For example, the constant density line of 1000 cm^{-3} on the layer bottom rapidly recovers upward before midday when there is still solar illumination. This implies that the photolysis reactions driven by solar radiation is not the most critical factor responsible for the significant bottom extensions and enhancements of Na layer below 75 km observed in mid-December, 2014.

According to the Na neutral chemical reactions (R1, R3), Na density evolution on the layer bottom are strongly dependent on temperature as well as the concentrations of background minor chemical constituents (e.g., O_3, H and O). Thus we analyze their variations in December, 2014, which are shown in Figures 3a-f, respectively. Figures 3a-b plot the daily mean temperature variation averaged in the altitude range of 70-75 km and 35-45 km, respectively, in December, 2014 from the SABER instrument. The red dotted lines represent the zonal mean (35-45 °N) results, the blue solid lines represent the results averaged over latitudes of 35-45 °N and longitudes of 110-120 °E, i.e., taking the averaged measurement profiles of the lidar site overpasses within a range of $\sim\pm5$° in latitude and $\sim\pm5$° in longitude. As can be seen, there are apparent temperature anomalies with opposite phase between upper stratosphere and upper mesosphere in mid-December over the lidar site (blue solid lines with asterisks), when compared to the zonal mean temperature (red solid lines with pluses). The temperature in

the altitude region of 70-75 km over the lidar site is increased by nearly 30 K within one week. During the same period (December 15-20), the local stratosphere shows ~15-20 K cooler than the zonal mean temperatures between 35 and 45 km.
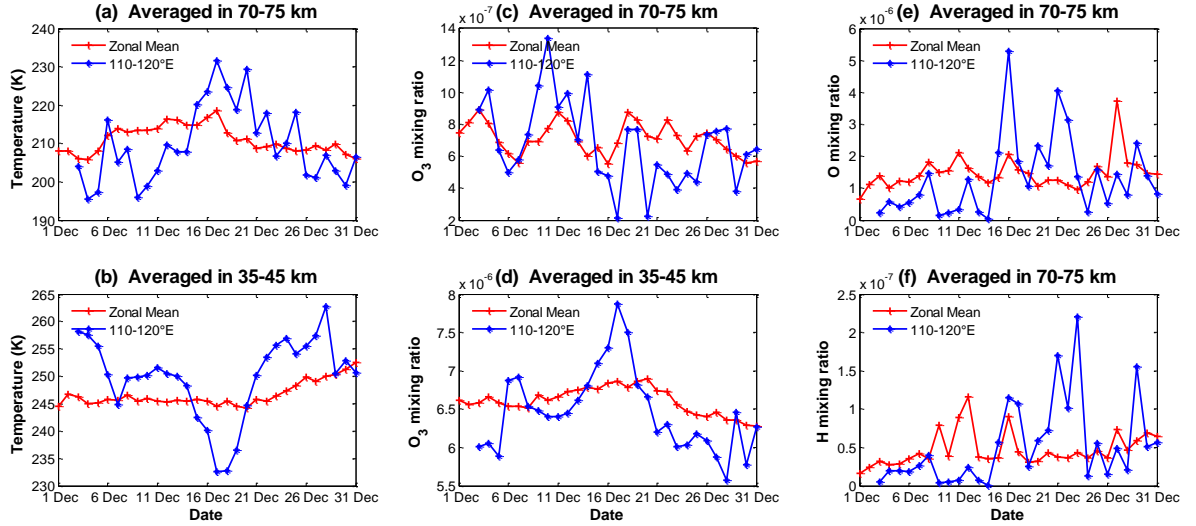
Figure 3: (a, b) Temperature variations in December, 2014 from the SABER instrument onboard TIMED satellite, averaged in the altitude range of 70-75 km and 35-45 km, respectively. (c, d) The same as (a-b) but for mixing ratio of O$_3$. (e, f) The variations of mixing ratio of atomic H and O in December, 2014 from SABER, averaged in the altitude range of 70-75 km. The red lines with pluses in each plot represent the daily and zonal mean results averaged between 35°N and 45°N, and the blue lines with asterisks represent the daily mean results averaged near the lidar site (35-45°N, 110-120°E).

The variations of Na chemistry-related background atmospheric species (e.g., O$_3$, H and O) can also be obtained from TIMED-SABER instrument (Figures 3c-f). Compared to the temporal variation of zonal mean value, the averaged O$_3$ mixing ratio near the lidar site (35-45°N, 110-120°E) shows weak negative perturbation between 70 and 75 km, while positive perturbation between 35 and 45 km in mid-December. Clear positive perturbations of the mixing ratios of atomic H and O averaged between 70 and 75 km over the lidar site are also observed in mid-December. For example, the mixing ratio of atomic H is increased by over 5 times on December 17 (from less than 0.2×10^{-7} to over 1×10^{-7}), as shown in Figure 3f. It is intriguing that the duration of background atmospheric anomalies over the lidar site (Figures 3a-f) coincides well with that of the significant Na density enhancement below 75 km shown in Figure 1. This implies that the neutral chemistry reaction (R3) makes a critical contribution to the observed Na enhancements on the layer bottom in mid-December. With a temperature of T=230 K (corresponding to a rate of R$_3\approx1.6\times10^{-13}$ cm^3 molecule^{-1} s^{-1}) and H density of 1×10^8 cm^{-3} (estimated according to the mixing ratio of atomic H and atmospheric density in the region between 70 and 75 km), the production rate of Na via reaction of NaHCO$_3$ with H is estimated to be increased by nearly 10 times compared with that under the typical mesopause atmospheric condition in winter of middle latitude in Northern Hemisphere (T=200 K, R$_3\approx7.2\times10^{-14}$ cm^3 molecule^{-1} s^{-1}, and assuming atomic H concentration to be 2×10^7 cm^{-3} between 70 and 75 km). Furthermore, considering the contribution by increase in atomic O and decrease in O$_3$ concentration near mesopause region, which facilitate the liberation of Na atoms and

restrict the removal of Na atoms via oxidation reaction respectively (Plane et al., 2015), the net production rate of atomic Na through neutral chemical reactions is expected to be faster than the estimation. Therefore, the neutral chemical reactions, accelerated by warming of upper mesosphere and increase of atomic H and O concentrations, play a critical role in the significant bottom extensions and enhancements of the Na layer below 75 km in mid-December. Undoubtedly, the photolysis of NaHCO$_3$ also contributes to the intense bottom extension of the Na layer after sunrise.
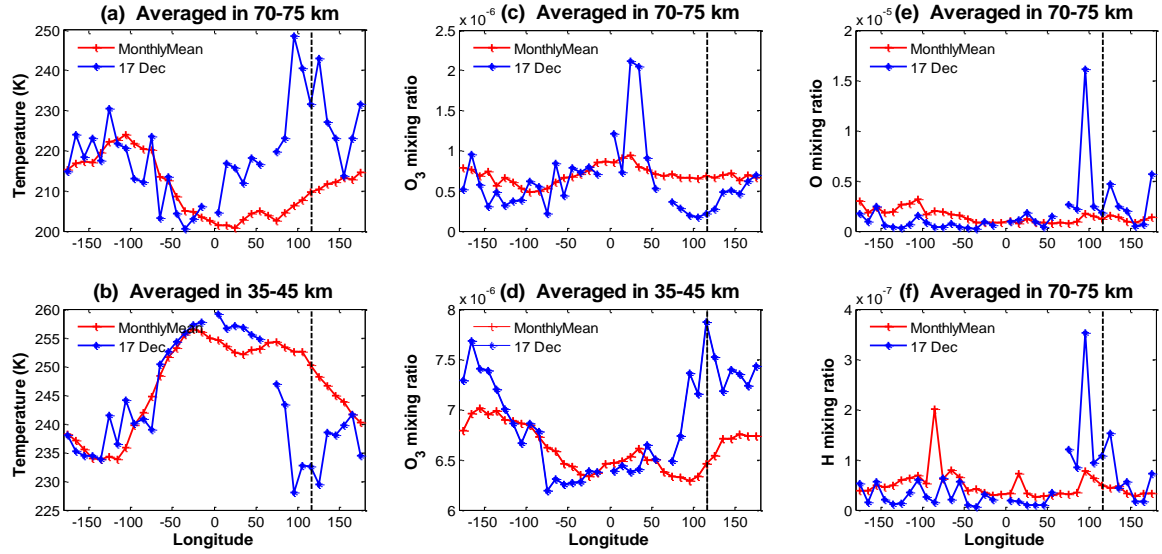
Figure 4: (a, b) Temperature variation with longitude, averaged between 35-45°N in the altitude range of 70-75 km and 35-45 km, respectively. (c, d) The same as (a-b) but for mixing ratio of O$_3$. (e, f) The variations of mixing ratio of atomic H and O with longitude, averaged between 35-45°N in the altitude range of 70-75 km. The red lines with pluses represent the monthly mean results in December, 2014, and the blue lines with asterisks represent the daily mean results on December 17. The black dotted lines in each plot indicate the longitude of the lidar site. Each data point is obtained by averaging within a longitude range of 10°.

These anomalous structures in background atmosphere over the lidar site appearing in mid-December, 2014 can be further verified in Figure 4. Figures 4a-b show the longitudinal variations of temperature averaged between 35-45°N in the altitude range of 70-75 km and 35-45 km, respectively. The red lines with pluses and blue lines with asterisks represent the monthly and daily (taking December 17 for example) mean results, respectively. The monthly mean temperatures in both the upper mesosphere and stratosphere regions show a wavy structure of zonal wavenumber 1. In Figures 4a-b, apparent anomalous temperature structures with opposite phase between the upper mesosphere and the stratosphere are seen on December 17 compared to the monthly mean results, and this extends across a longitude range of nearly 100°, covering the lidar site (116.01°E). The longitudinal variations of minor chemical constituents averaged between 35-45°N are plotted in Figures 4c-f, respectively. Similarly, negative perturbations of O$_3$, and positive perturbations of atomic H and O averaged in the altitude range of 70-75 km near the lidar site can be clearly seen in the daily mean results on December 17.
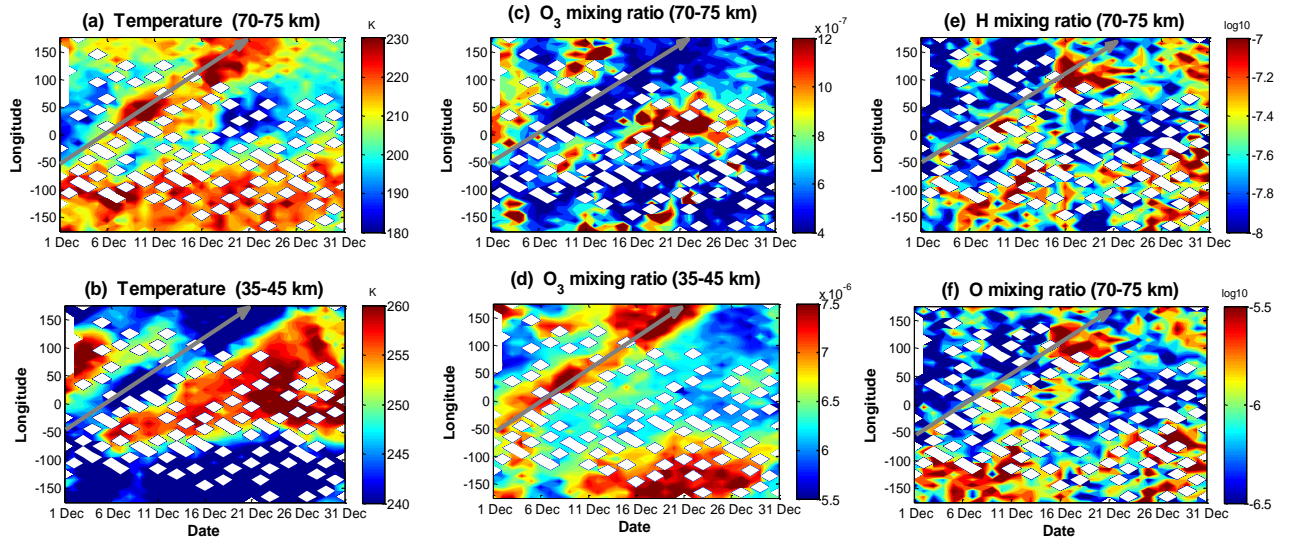
Figure 5: (a-d) The temporal variations of temperature and O₃ with longitude averaged over 35-45 °N and in the altitude range of 70-75 km and 35-45 km, respectively. **(e-f)** The daily variations of atomic H and O with longitude, averaged over 35-45 °N and in the altitude range of 70-75 km, respectively.

The synchronous and out-of-phase atmosphere anomalies between the upper stratosphere and mesosphere over the lidar site in mid-December, together with the fact that these anomalies lasted for several days, imply that they are most likely linked to PW activities. Figure 5 shows the temporal-longitudinal variations in temperature and neutral chemical species averaged in 35-45 °N in the upper stratosphere (35-45 km) and the upper mesosphere (70-75 km) in December, 2014 observed by SABER/TIMED. Figures 5a-f show clear eastward planetary-scale perturbations in these background atmospheric parameters, and the atmospheric anomalies appearing in mid-December near the Na lidar site are shown to be the result of the zonal shifting perturbation structure transporting from west to east.

It is worth mentioning that the cooling anomaly in the stratosphere and warming anomaly in the mesosphere are exactly the opposite of the temperature anomalies observed during the well-known sudden stratosphere warming (SSW) event appearing in high latitudes. Yuan et al. (2012) reported that a significant decrease in Na abundance below 90 km was observed at 41 °N during the 2009 SSW event, which is consistent with the dramatic cooling in this region. Feng et al. (2017) also investigated the responses of metal layers to the 2009 major SSW, and substantial depletions of the Na and Fe layers were seen both from the lidar measurements and model simulations mainly due to the mesospheric cooling. Sudden enhancement of PWs and their interactions with the mean flow are widely accepted as the cause of SSWs (Matsuno, 1971). We further use ERA-Interim reanalysis to calculate the longitudinal distributions of geopotential amplitudes of PWs in the stratosphere. Figure 6 shows the zonal distribution of geopotential height amplitudes (Unit: gpm) at 10 hPa (~32 km) and 45 °N in December, 2014. It can be seen that before mid-December, planetary wave number 2 (PW2) is unusually strong and the amplitude of PW2 is even larger than that of PW1. The PW2 trough (low geopotential height associated with cold air) moves eastward to the longitude of the lidar site (~116 °E) near Dec 15, resulting that this region was dominated by cold air

275 mass. After Dec 17, the amplitude of PW2 significantly decreases and PW1 increases. PW1 ridge (high geopotential height associated with warm air) starts to dominate the region near the lidar site. This demonstrated that the atmospheric temperature anomalies in the stratosphere in mid-December, 2014 around the lidar region was indeed related to the unusual PW activity. According to Smith (1996), the planetary-scale disturbances might be generated in-situ by longitudinal variations of gravity wave (GW) forcing in the mesosphere due to the GW filtering by PWs in the stratosphere. The opposite

280 phase of anomalies between the stratosphere and mesosphere are likely caused by the interaction with gravity waves (GWs) (Limpasuvan et al., 2012). It is noted that indeed a minor SSW occurred about half a month later (in early January, 2015). However, a detailed investigation on this aspect is beyond the scope of the present work.
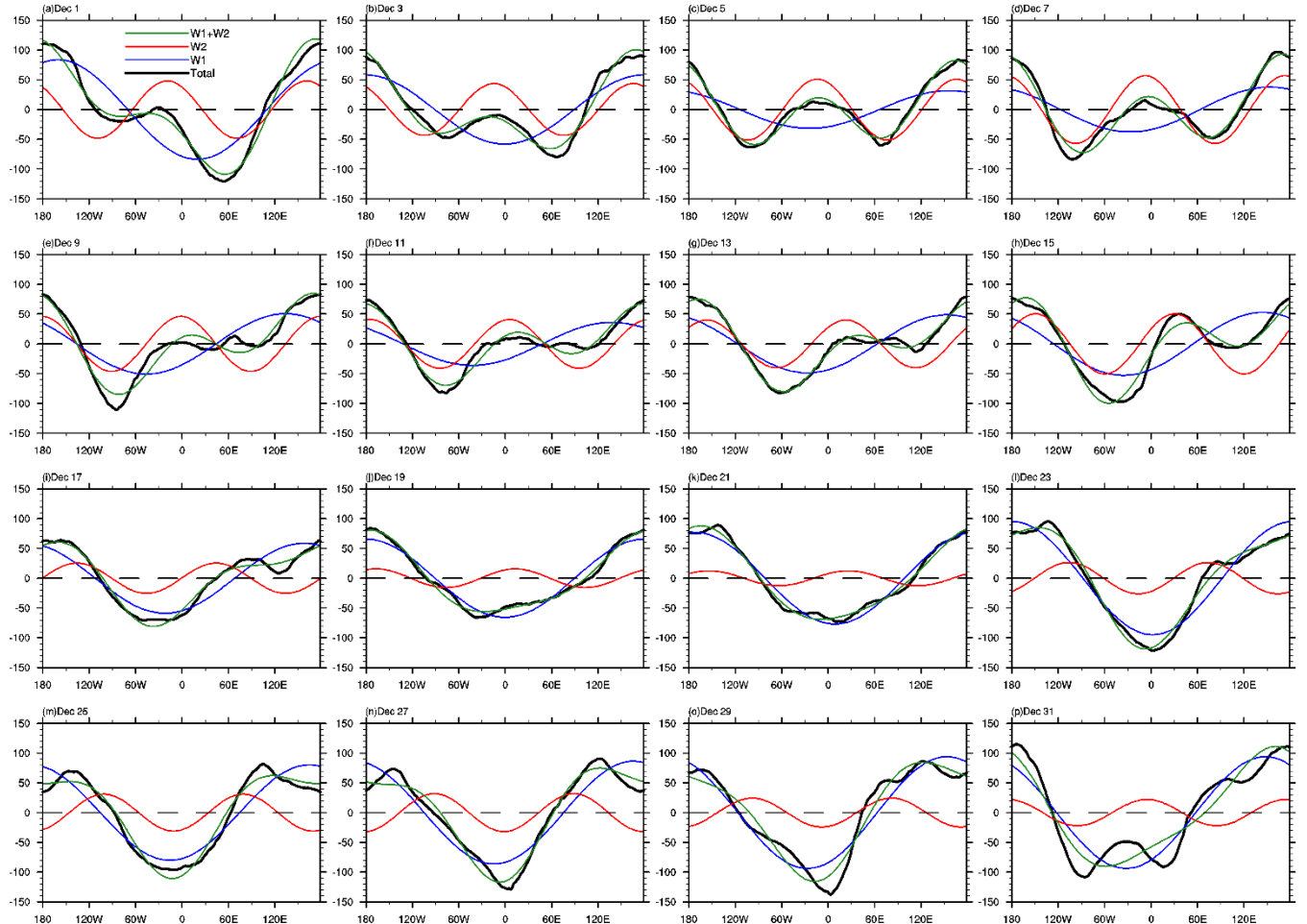
Figure 6: Longitudinal distributions of geopotential amplitudes of PWs for Dec. 1~31, 2014 (shown on every other day; Black:
285 **total; Blue: PW1; Red: PW2; Green: PW1+PW2).**
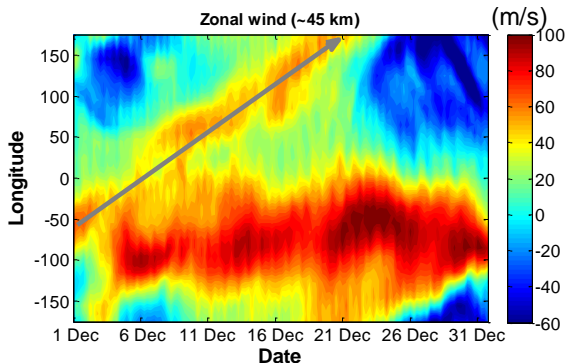
Figure 7: The temporal variation of zonal wind with longitude, averaged over 35-45 N near 45 km obtained from ERA-Interim global atmospheric reanalysis data.
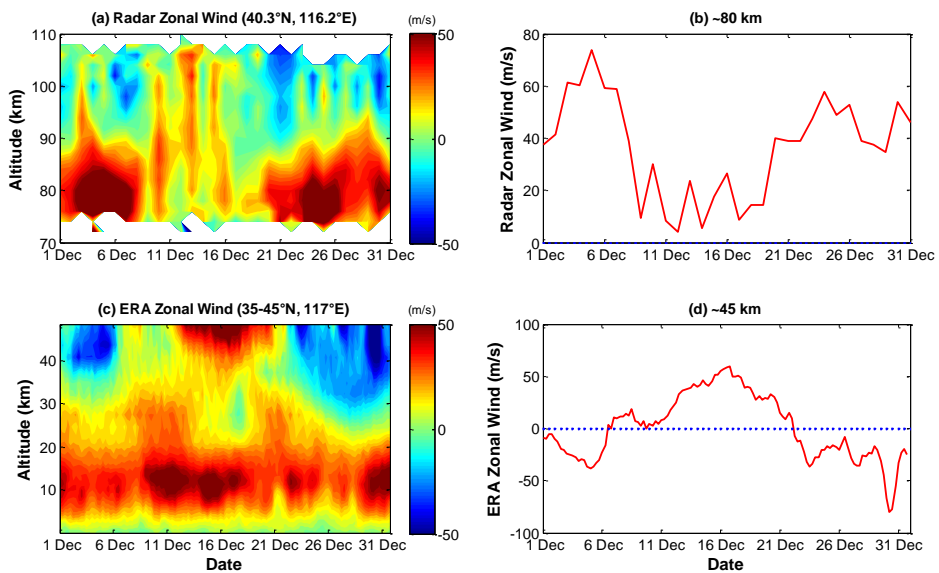
Figure 8: (a, c) The temporal variations of zonal wind with altitude near the lidar site in December, 2014 obtained from meteor radar (70-110 km, 40.3 N,116.2 E) and ERA reanalysis data (0-48 km, 35-45 N,117 E), respectively; (b, d) The temporal variations of zonal wind near 80 km and 45 km, respectively(red lines). The blue dashed lines indicate zero wind.

The stratosphere zonal wind, averaged over 35-45 N near 45 km obtained from ERA-Interim global atmospheric reanalysis also exhibit eastward transporting structure of westerly wind, which is consistent with the temporal-longitudinal variation of temperature and minor constituents in December 2014 (as indicated by the grey arrow in Figures 5 and 7). As shown in Figures 8a-b, the zonal wind results observed by a meteor radar located near the lidar site reveal apparent westerly wind deceleration of over 50 m/s in the upper mesosphere region near 80 km, and simultaneous easterly wind reversal above 90 km in mid-December. During almost the same time period, the zonal wind in the upper stratosphere changes direction from easterly to westerly (Figures 8c-d). In late December, the zonal wind in the upper mesosphere and the upper stratosphere recovers to the large westerly wind and easterly wind, respectively. The zonal wind reversal from westward to

eastward in the upper stratosphere and deceleration of eastward zonal wind in the upper mesosphere in mid-December are close in time to the appearance of the anomalies of temperature and minor chemical constituents over the lidar site.

Previous works have demonstrated the importance of the stratosphere wind filtering in controlling the propagation of atmospheric waves to the upper mesosphere region (e.g., Siskind et al., 2010). The out-of-phase temperature anomalies in the upper stratosphere and upper mesosphere in mid-December hint their coupling likely through interaction of PW with mean-flow and changing the GW filtering by the stratospheric wind. The westerly zonal wind in the stratosphere (as shown in Figure 7 and 8(c)) can induce filtering of eastward-propagating GWs and penetration of westward-propagating GWs into the mesosphere (Chandran et al., 2011). The westward-propagating GWs induces a downward circulation in the mesosphere causing adiabatic heating (Liu and Roble, 2002, 2005; Yamashita et al., 2010). Therefore, the dramatic cooling and heating in the stratosphere and the mesosphere in mid-December are likely caused by the perturbations of PWs and their interaction with GWs (Marsh, 2011, 2013; Limpasuvan et al., 2012 and references therein). The strong perturbations of O_3 with zonal shift in the stratosphere and upper mesosphere (Figures 5c-d) are likely to be linked to the consistent temperature perturbations (Figures 5a-b). The reaction rate of O_3 production ($O+O_2+ M \rightarrow O_3+M$) increases with decreasing temperature (Smith and Marsh, 2005), thus the decrease of temperature in the stratosphere shifts the O/O_3 ratio towards O_3, resulting in the increase of O_3. And then the upper mesosphere becomes in the opposite situation to that in the stratosphere. The temporal variation of atomic H and O with longitude (Figures 5e-f) did not show as obvious zonal shifting structures as seen in O_3. The strong positive perturbations of atomic H and O in the upper mesosphere over the lidar site in mid-December might be also partly associated to the downwelling in the upper mesosphere, which could force H- and O-rich air downward and increase the concentrations of H and O below 80 km as their mixing ratios increase with altitude near 80 km (Marsh et al., 2013; Narayanan et al., 2021). Near 80 km, the vertical gradients of both atomic O and H are very large (as shown in Figures 9a-b). The positive perturbations in H and O below 80 km in the mid-December are also clearly seen in Figures 9c-d, which obtained by subtracting the monthly mean vertical profiles from the temporal and altitude variations of mixing ratios of H and O.
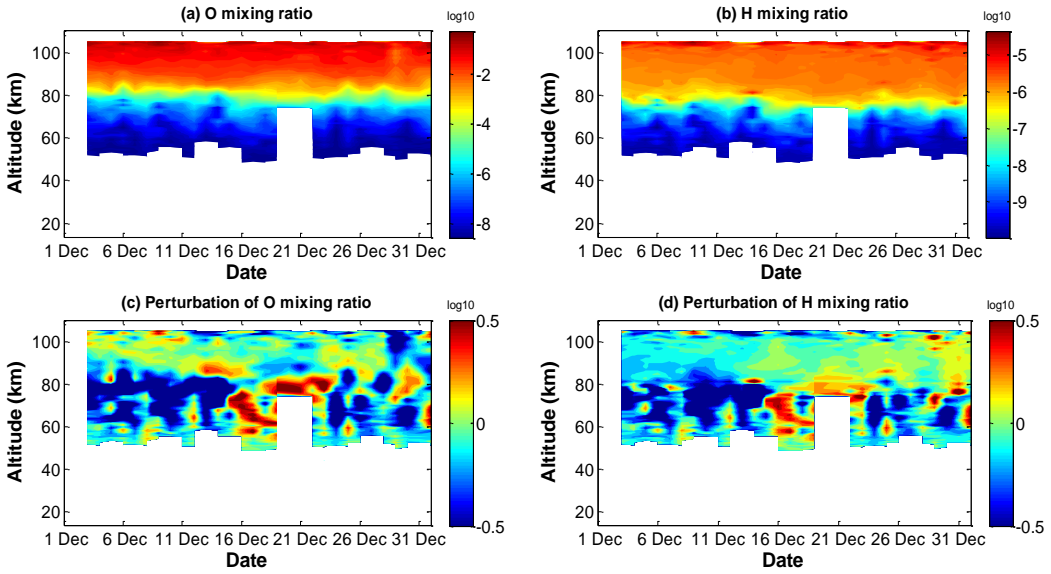
Figure 9: (a, b) The temporal and altitude variations of mixing ratio (in logarithm coordinates) of atomic O and H obtained from SABER/TIMED. The data within 35-45 ˚N and 110-120 ˚E was averaged. (c, d) Their perturbations obtained by subtracting the monthly mean vertical profiles.

Comparing the behavior of Na layer on December 17 to that on December 14 and 18, the most striking feature for the former is the more apparent wavy structures with downward propagation phase. It is worth mentioning that the aircraft Na lidar during the Deep Propagating Gravity Wave Experiment (DEEPWAVE) measurement program observed multiple Na layers descending to 70-72 km over New Zealand in 2014 due to mountain waves (MWs) (Bossert et al., 2015, 2018; Fritts et al., 2016, 2018). The downwelling regions in Figure 2a seem to repeat on multiple days and are likely due to the superposition of tide and GW. The waves can induce adiabatic vertical motion of the air parcel, leading to adiabatic heating and thereby contributing to the much stronger Na layer bottom enhancement on Dec 17. In the absence of chemistry, the GW/tide-induced temperature perturbation due to adiabatic expansion and compression of the air parcel can be approximately calculated according to the vertical displacements of Na mixing ratio isopleths based on the approach in Bossert et al. (2015, 2018). Figure 10a shows the Na mixing ratio contours corresponding to Figure 2a. The isopleth highlighted in red corresponds to 1×10^{-12} and an average altitude of 77.01 km. In Bossert et al. (2018), the average altitude of each isopleth was used as the undisturbed equilibrium altitude for the temperature perturbation calculation. However, it is unreasonable to use the average altitude (~77.01 km) of the highlighted isopleth here because the observation is diurnal (nearly 44 h), and the Na mixing ratio is largely affected by photochemistry. If we choose the isopleth between 22 and 24 LT (before the descending layer formation) on Dec 17, the average altitude is calculated to be 78.74 km, and the corresponding temperature perturbation for the highlighted isopleth in Figure 10a is shown in Figure 10b. Taking into account the chemistry which depends strongly on temperature, Bossert et al. (2018) employed a model of Na chemistry to determine the chemical amplification factor (CAF) of atomic Na. The CAF was then used to correct the calculated temperature

perturbations from Na mixing ratio. For a mean height of 81.5 km and a wave with period of 20 min was turned on one hour after sunset, the largest CAF of atomic Na is ~1.6 within 4 hours after sunset. However, the effect of chemistry on the underside of the Na layer would be greater during daytime. After sunrise, solar radiation will significantly accelerate the photolysis reaction of $NaHCO_3$, and convert $NaHCO_3$ back to Na atoms (R2). In addition, the photolysis of O_2, O_3 and H_2O during the day can greatly increase the concentrations of atomic O and H around and below 80 km (Plane, 2003), thus further promoting the release of Na atoms from $NaHCO_3$ (R3) or NaO and NaO_2. Therefore the CAF will increases significantly and be much larger than 1.6 after sunrise, especially at lower altitudes (i.e., below 80 km). The GW-induced adiabatic temperature perturbations on Dec 17 would be much smaller than the roughly estimated values shown in Figure 10b. In order to properly estimate the adiabatic temperature change associated with the downwelling forced by the superposition of GW and tide, a more comprehensive model investigation may be needed.

Actually, before the strong downwelling regions appear, the SABER sampling profile obtained at ~20:58 LT on Dec 16 around the lidar site already shows considerable positive perturbations (~30 K) at around 75 km, as shown in Figure 11b. The temperature profiles obtained at ~00:26 and 02:03 LT on Dec 17 (Figure 11c-d) also have warming anomalies around 75 km. However, the Na mixing ratio isopleths moved down to below 80 km after ~4 LT. The temperature anomalies also appeared on other days near mid-December (e.g., Dec 14, 18, as shown in Figure 11a, f). These imply that the temperature perturbations near 75 km observed by SABER are more likely linked to the GW filtering by PW rather than the strong downwelling caused by the superposition of tide and GW.

Given all of that, we suggest two causes for inducing adiabatic heating and contributing to the observed more significant bottom enhancement on December 17. One is the interaction of PW with mean flow which could change GW filtering properties by the stratospheric wind (Yamashita et al., 2010; Liu and Roble, 2002). This occurs over a relatively large horizontal area as seen in Figures 4 and 5 (covering nearly 50 ° in longitude around the lidar site and lasting several days in mid-December, i.e., on Dec 14, 18, in addition to Dec 17). The other is the superposition of tide and GW, which induces the stronger downwelling on Dec 17 as shown in Figure 2. The effect of the latter is more significant than the former as we see the bottom enhancement on Dec 17 is much more pronounced than that observed on Dec 14 and 18.
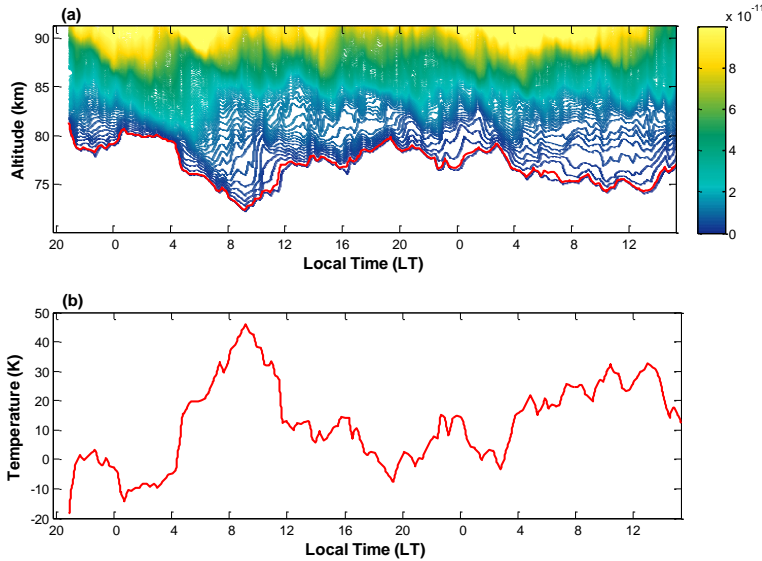
370

Figure 10: (a) Na mixing ratio corresponding to Figure 2(a); (b) Adiabatic vertical motion-induced temperature perturbations calculated from the highlighted Na mixing ratio isopleth (1×10^{-12}) in (a).
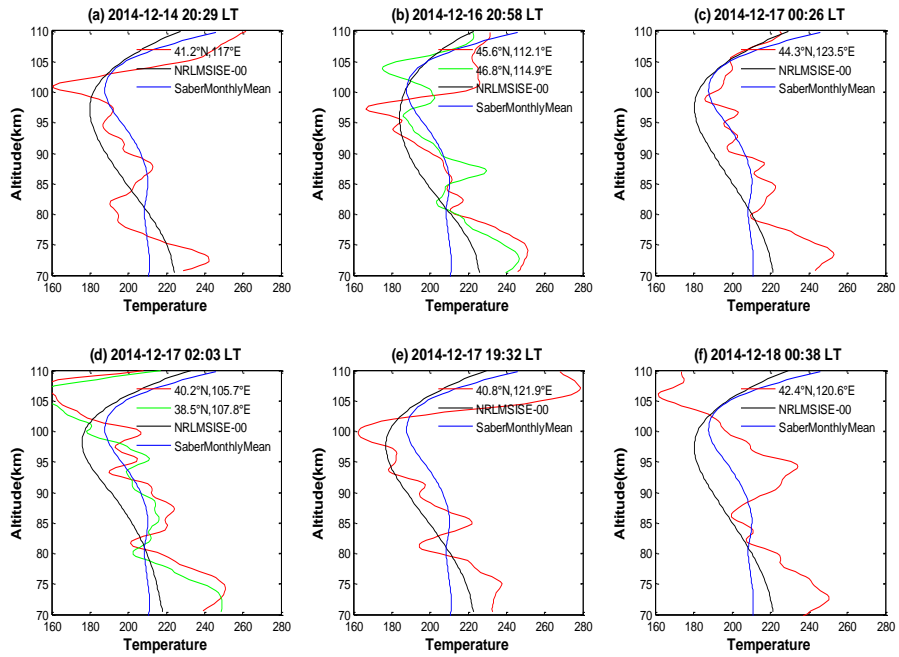
Figure 11: SABER temperature profiles obtained near the lidar location. Blue and black lines in each subplot represent the

375 **temperature profiles from NRLMSISE-00 and monthly average SABER results near the lidar location, respectively.**

5 Conclusions

In this study, we report the observations of significant extension of Na layer bottom by a diurnal Na lidar in mid-December, 2014 at Beijing (40.41 °N, 116.01 °E), China. Considerable Na atoms are observed even as low as ~72 km. Liberation of Na atoms from its reservoir (e.g., $NaHCO_3$) near the Na layer bottom via neutral chemical reactions, which are accelerated by the largely increased temperature and concentrations of atomic H and O, is suggested to be the critical production mechanism of the enhanced Na layer below 75 km. The diurnal lidar measurements of the Na layer, zonal wind results from a nearby meteor radar, global satellite observations as well as reanalysis data presented here reveal the close correlation between the variation of Na layer bottom and planetary scale atmospheric processes. The longitudinal distributions of geopotential amplitudes of PW show that there exists unusual development of the amplitude of PW2, and the stratosphere near the lidar location is dominated by PW2 trough in mid-December. The out-of-phase temperature anomalies in the upper stratosphere and upper mesosphere are likely due to the modulation of GW filtering by stratosphere wind. The strong eastward wind in the upper stratosphere provides a favorable condition for the vertical propagation of westward GWs. Westward forcing could induce a poleward flow and drive downward circulation in the mesosphere, leading to adiabatic heating. The unprecedented Na density of ~2500 cm^{-3} near 75 km observed on December 17, 2014 is also greatly contributed by the adiabatic vertical motion of air parcel forced by the superposition of tide and GW.

The results of this paper provide direct observational evidence for the role of PWs in the perturbations of metal layers in the upper mesosphere region. These results also have implications for the response of the metal layers (especially the layer bottom) to perturbations in the lower atmosphere (i.e., stratosphere). Modeling studies are desirable to investigate the complicated interactions of dynamical and chemical processes and their effects on the variations of metal layer in more depth.

Data availability. The SABER/TIMED data used in this study are downloaded from http://saber.gats-inc.com/browse_data.php (last access: May 2022). The ERA reanalysis data used in this study were obtained from https://www.ecmwf.int/en/forecasts/datasets/archive-datasets/ (last access: May 2022). The MERRA-2 data were obtained from the National Aeronautics and Space Administration, Goddard Space Flight Center, Atmospheric Chemistry and Dynamics Laboratory (NASA GFC ACDL) site at https://acd-ext.gsfc.nasa.gov/Data_services/ met/ann_data.html (last access: June 2020). The meteor radar data were supported by the Chinese Meridian Project and are available from Beijing National Observatory of Space Environment, Institute of Geology and Geophysics Chinese Academy of Sciences through the Geophysics center, National Earth System Science Data Center (http://wdc.geophys.ac.cn, last access: March 2020). The datasets collected from the diurnal Na lidar measurements above Beijing, China, are available upon request to G.T. Yang (gtyang@nssc.ac.cn).

Author contributions. YX carried out the data analysis and wrote the manuscript. JJ and SN contributed to the discussion of the results and the preparation of the manuscript. XWC, JHW and FQL supported operations of the lidar and took part in the

discussions. CHS contributed to the discussion of planetary wave activity and performed data analysis of geopotential
410 amplitudes of planetary waves in the revised manuscript. LFD and HRZ were responsible for the lidar operations. YJL
contributed to the analysis of reanalysis data. GTY conceived this study and contributed to the discussion of the results.

Competing interests. The authors declare that they have no conflict of interest.

415 *Acknowledgments.* This work was supported by the National Natural Science Foundation of China (No. 41627804,
41604130), the Natural Science Foundation of the Jiangsu Higher Education Institutions of China (21KJB510007,
20KJD170001). This work was also supported in part by the Specialized Research Fund and the Open Research Program of
the State Key Laboratory of Space Weather. We acknowledge the use of the data from the Chinese Meridian Project
(http://data.meridianproject.ac.cn/), and the Geophysics center, National Earth System Science Data Center. A part of this
420 work was carried out while YX visited Institute for Space-Earth Environmental Research (ISEE) under the International
Joint Research program of ISEE, Nagoya University. The authors would like to thank Prof. X.Z. Chu for valuable
suggestions and helpful discussion.

References

Bossert, K., D. C. Fritts, P.-D. Pautet, B. P. Williams, M. J. Taylor, B. Kaifler, A. Dornbrack, I.M. Reid, D.J. Murphy, A.J.
425 Spargo, and A.D Mackinnon: Momentum flux estimates accompanying multiscale gravity waves over Mount Cook,
New Zealand, on 13 July 2014 during the DEEPWAVE campaign, J. Geophys. Res., 120, 9323–9337,
https://doi.org/10.1002/2015JD023197, 2015.

Bossert, K., D. C. Fritts, C. J. Heale, S. D. Eckermann, J. M. C. Plane, J. B. Snively, B.P. Williams, I.M. Reid, D.J. Murphy,
A.J., Spargo, and A.D. Mackinnon: Momentum flux spectra of a mountain wave event over New Zealand, J. Geophys.
430 Res.-Atmos, 123, 9980-9991, https://doi.org/10.1029/2018JD028319, 2018.

Chen, H., White, M. A., Krueger, D. A., and She, C. Y.: Daytime mesopause temperature measurements using a sodium-
vapor dispersive Faraday flter in lidar receiver, Opt. Lett., 21, 1093–1095, 1996.

Cox, R. M., Self, D. E., and Plane, J. M. C.: A study of the reaction between NaHCO3 and H: apparent closure on the neutral
chemistry of sodium in the upper mesosphere, J. Geophys. Res., 106, 1733–1739, 2001.

435 Clemesha, D. M., Batista, P. P., and Simonich, D. M.: Tide-induced oscillations in the atmospheric sodium layer, J. Atmos.
Sol.-Terr.Phys., 64, 1321–1325, 2002.

Chandran, A., Collins, R. L., Garcia, R. R., and Marsh, D. R.: A case study of an elevated stratopause generated in the
Whole Atmosphere Community Climate Model, Geophys. Res. Lett., 38, L08804, https://doi.org/10.1029/2010GL046566,
2011.

440   Feng, W., B. Kaifler, D. R. Marsh, J. Hoffner, U.-P. Hoppe, B. P. Williams, J. M. C. Plane: Impacts of a sudden stratospheric warming on the mesospheric metal layers, J. Atmos. Sol. Terr. Phys., 162, 162–171, http://doi.org/10.1016/j.jastp.2017.02.004, 2017.

Fritts, D. C., R. B. Smith., M. J. Taylor, J. D. Doyle, S. D. Eckermann, A. Dornbrack et al.: The Deep Propagating Gravity Wave Experiment (DEEPWAVE): An Airborne and Ground-Based Exploration of Gravity Wave Propagation and Effects

445   from their Sources throughout the Lower and Middle Atmosphere, Bull. Am. Meteorol. Soc., https://doi.org/10.1175/BAMS-D-14-00269.1, 2016.

Fritts, D. C., S. B. Vosper, B. P. Williams, K. Bossert, J. M. C. Plane, M. J. Taylor, P. D. Pautet, S. D. Eckermann, C. G. Kruse, R. B. Smith, A. Dornbrack, M. Rapp, T. Mixa, I. M. Reid, D. J. Murphy: Large-amplitude mountain waves in the mesosphere accompanying weak cross-mountain flow during DEEPWAVE Research Flight RF22, J. Geophys. Res.-

450   Atmos., 123, https://doi.org/10.1029/2017JD028250, 2018.

Gardner, C. S., and Liu, A. Z.: Wave-induced transport of atmospheric constituents and its effect on the mesospheric Na layer, J. Geophys. Res., 115, D20302, https://doi.org/10.1029/2010JD014140, 2010.

Gao, Q., Chu, X., Xue, X., Dou, X., Chen, T., Chen, J.: Lidar observations of thermospheric Na layers up to 170 km with a descending tidal phase at Lijiang (26.7°N, 100.0°E), China, J. Geophys. Res., 120: 9213–9220, 2015.

455   Gómez Martín, J. C., Garraway, S. A., and Plane, J. M. C.: Reaction Kinetics of Meteoric Sodium Reservoirs in the Upper Atmosphere, J. Phys. Chem. A., 120, 1330–1346, https://doi.org/10.1021/acs.jpca.5b00622, 2016.

Jiao, J., Yang, G., Wang, J., Cheng, X., Li, F., Yang, Y., Gong, W., Wang, Z., Du, L., Yan, C., Gong, S.: First report of sporadic K layers and comparison with sporadic Na layers at Beijing, China (40.6∘N, 116.2∘E), J. Geophys. Res., 120, 5214–5225, https://doi.org/10.1002/ 2014JA020955, 2005.

460   Liu, H. L., and Roble, R. G.: A study of a self-generated stratospheric sudden warming and its mesospheric/lower thermospheric impacts using coupled TIME-GCM/CCM3, J. Geophys. Res., 107(D23), 4695, https://doi.org/:10.1029/2001JD001533, 2002.

Liu, H. L., and Roble, R. G.: Dynamical Coupling of the stratosphere and mesosphere in the 2002 Southern Hemisphere major stratospheric sudden warming, Geophys. Res. Lett., 32, L13804, 2005.

465   Limpasuvan, V., Richter, J. H., Orsolini, Y. J., Stordal, F., Kvissel, O. K.: The roles of planetary and gravity waves during a major stratospheric sudden warming as characterized in WACCM, J. Atmos. Solar-Terr. Phys., 78–79, 84–98, http://dx.doi.org/10.1016/j.jastp.2011.03.004, 2012.

Matsuno, T.: A dynamical model of the stratospheric sudden warming, J. Atmos. Sci., 28, 1479– 1494, 1971.

Marsh, D.: Chemical-dynamical coupling in the Mesosphere and Lower Thermosphere, In: Abdu, M., Pancheva, D.,

470   Bhattacharyya, A. (Eds.), Aeronomy of the Earth's Atmosphere and Ionosphere, IAGA Special Sopron Book Ser., vol. 2, first ed., 370 pp., ISBN: 978–94–007–0325–4, Springer, Dordrecht, 2011.

Marsh, D. R., Janches, D., Feng, W., and Plane, J. M. C.: A global model of meteoric sodium, J. Geophys. Res.-Atmos., 118, 11442–11452, https://doi.org/10.1002/jgrd.50870, 2013.

Narayanan, V.L., Nozawa, S., Oyama, S., Mann, I., Shiokawa, K., Otsuka, Y., Saito, N., Wada, S., Kawahara, T. D., and

475 Takahashi, T.: Formation of an additional density peak in the bottom side of the sodium layer associated with the passage of multiple mesospheric frontal systems, Atmos. Chem. Phys., 21, 2343–2361, https://doi.org/10.5194/acp-21-2343-2021, 2021.

Plane, J. M. C., Cox, R. M., and Rollason, R. J.: Metallic layers in the mesopause and lower thermosphere region, Adv. Space Res., 24, 1559–1570, 1999.

480 Plane, J. M. C.: Atmospheric chemistry of meteoric metals, Chem. Rev., 103, 4963–4984, https://doi.org/10.1021/cr0205309, 2003.

Plane, J. M. C.: A time-resolved model of the mesospheric Na layer: constraints on the meteor input function, Atmos. Chem. Phys., 4, 627–638, https://doi.org/10.5194/acp-4-627-2004, 2004.

Plane, J. M. C., Feng, W., and Dawkins, E. C.: The Mesosphere and Metals: Chemistry and Changes, Chem. Rev., 115,

485 4497–4541, https://doi.org/10.1021/cr500501m, 2015.

Russell III, J.M., Mlynczak, M.G., Gordley, L.L., Tansock, J.J.J., Esplin, R.W.: Overview of the SABER experiment and preliminary calibration results, SPIE, 277–288, http://dx.doi.org/10.1117/12.366382, 1999.

Rienecker, M. M., Suarez, M. J., Gelaro, R., Todling, R., Bacmeister, J., Liu, E., Bosilovich, M. G., Schubert, S. D., Takacs, L., Kim, G.-K., Bloom, S., Chen, J., Collins, D., Conaty, A., da Silva, A., Gu, W., Joiner, J., Koster, R. D., Lucchesi, R.,

490 Molod, A., Owens, T., Pawson, S., Pegion, P., Redder, C. R., Reichle, R., Robertson, F. R., Ruddick, A. G., Sienkiewicz, M., and Woollen, J.: MERRA: NASA's modern-era retrospective analysis for research and applications, J. Climate, 24: 3624–3648, 2011.

Smith, A. K.: Longitudinal variations in mesospheric winds: Evidence for gravity wave filtering by planetary waves, J. Atmos. Sci., 53, 1156–1173, 1996.

495 States, R. J., Gardner, C. S.: Structure of the mesospheric Na layer at 40◦ N latitude: seasonal and diurnal variations, J. Geophys. Res., 104, 11783–11798, 1999.

Self, D. E., and Plane, J. M. C.: Absolute photolysis cross-sections for NaHCO$_3$, NaOH, NaO, NaO$_2$ and NaO$_3$: Implications for sodium chemistry in the upper mesosphere, Phys. Chem. Chem. Phys., 4, 16–23, https://doi.org/10.1039/B107078A, 2002.

500 Smith, A. K. and Marsh, D. R.: Processes that account for the ozone maximum at the mesopause, J. Geophys. Res.-Atmos.,110, D23305, https://doi.org/10.1029/2005JD006298, 2005.

Siskind, D. E., Eckermann, S. D., McCormack, J. P., Coy, L., Hoppel, K. W., Baker, N. L.: Case studies of the mesospheric response to recent minor, major, and extended stratospheric warmings, J. Geophys. Res., 115, D00N03, https://doi.org/10.1029/2010JD014114, 2010.

505 Smith, A. K., Garcia, R. R., Marsh, D. R., Richter, J. H.: WACCM simulations of the mean circulation and trace species transport in the winter mesosphere, J. Geophys. Res., 116, D20115, http://dx.doi.org/10.1029/2011JD016083, 2011.

Viehl, T. P., Plane, J. M. C., Feng, W., and Höffner, J.: The photolysis of FeOH and its effect on the bottomside of the mesospheric Fe layer, Geophys. Res. Lett., 43, 1373–1381, https://doi.org/10.1002/2015GL067241, 2016.

Wang, C.: New chains of space weather monitoring stations in China, Space Weather, 8, S08001, https://doi.org/10.1029/2010SW000603, 2010.

Xu, J., and A. K. Smith: Perturbations of the sodium layer: controlled by chemistry or dynamics? Geophys. Res. Lett., 30(20), 2056, 2003.

Xu, J., and A. K. Smith: Evaluation of processes that affect the photochemical timescale of the sodium layer. J. Atmos. Sol. Terr. Phys., 67, 1216-1225, 2005.

Xia, Y., Cheng, X., Li, F., Yang, Y., Lin, X., Jiao, J., Du, L., Wang, J., and Yang, G.: Sodium lidar observation over full diurnal cycles in Beijing, China, Appl. Optics, 59(6), 1529-1536, 2020.

Yamashita, C., H. L. Liu, and X. Chu: Responses of mesosphere and lower thermosphere temperatures to gravity wave forcing during stratospheric sudden warming, Geophys. Res. Lett., 37, L09803, doi:10.1029/2009GL042351, 2010.

Yu, Z., Chu, X., Huang, W., Fong, W., and Roberts, B. R.: Diurnal variations of the Fe layer in the mesosphere and lower thermosphere: Four season variability and solar effects on the layer bottomside at McMurdo (77.8°S, 166.7°E), Antarctica, J. Geophys. Res., 117, D22303, https://doi.org/10.1029/2012JD018079, 2012.

Yu, Y., Wan, W.X., Ning, B.Q., Liu, L.B., Wang, Z.G., Hu, L.H., Ren, Z.P.: Tidal wind mapping from observations of a meteor radar chain in December 2011, J. Geophys. Res-Space, 118, 2321–2332, http://dx.doi.org/10.1029/2012ja017976, 2013.

Yuan, T., B. Thurairajah, C.-Y. She, A. Chandran, R. L. Collins, and D. A. Krueger: Wind and temperature response of midlatitude mesopause region to the 2009 Sudden Stratospheric Warming, J. Geophys. Res., 117, D09114, doi:10.1029/2011JD017142, 2012.

Yuan, T., She, C.-Y., Kawahara, T. D., and Krueger, D. A.: Seasonal variations of mid-latitude mesospheric Na layer and its tidal period perturbations based on full-diurnal-cycle Na lidar observations of 2002–2008, J. Geophys. Res., 117, D1130, https://doi.org/10.1029/ 2011JD017031, 2012.

Yuan, T., Feng, W., Plane, J. M. C., and Marsh, D. R.: Photochemistry on the underside of the mesospheric Na layer, Atmos. Chem. Phys., 19, 3769–3777, https://doi.org/10.5194/acp-19- 3769-2019, 2019.